Biosensors and Bioelectronics 197 (2022) 113735

Contents lists available at ScienceDirect

Biosensors and Bioelectronics

journal homepage: www.elsevier.com/locate/bios

Aptasensing nucleocapsid protein on nanodiamond assembled gold interdigitated electrodes for impedimetric SARS-CoV-2 infectious disease assessment

Santheraleka Ramanathan [a], Subash C.B. Gopinath [a,b,*], Zool Hilmi Ismail [c,**], M. K. Md Arshad [a,d], Prabakaran Poopalan [d]

[a] Institute of Nano Electronic Engineering, Universiti Malaysia Perlis (UniMAP), 01000, Kangar, Perlis, Malaysia
[b] Faculty of Chemical Engineering Technology, Universiti Malaysia Perlis (UniMAP), 02600, Arau, Perlis, Malaysia
[c] Centre for Artificial Intelligence and Robotics, Universiti Teknologi Malaysia, Jalan Sultan Yahya Petra, 54100, Kuala Lumpur, Malaysia
[d] Faculty of Electronic Engineering Technology, Universiti Malaysia Perlis (UniMAP), 02600, Arau, Pauh Putra, Perlis, Malaysia

ARTICLE INFO

Keywords:
COVID-19
Biosensor
Biomarker
Respiratory virus
Pandemic
Corona virus

ABSTRACT

In an aim of developing portable biosensor for SARS-CoV-2 pandemic, which facilitates the point-of-care aptasensing, a strategy using 10 μm gap-sized gold interdigitated electrode (AuIDE) is presented. The silane-modified AuIDE surface was deposited with ~20 nm diamond and enhanced the detection of SARS-CoV-2 nucleocapsid protein (NCP). The characteristics of chemically modified diamond were evidenced by structural analyses, revealing the cubic crystalline nature at (220) and (111) planes as observed by XRD. XPS analysis denotes a strong interaction of carbon element, composed ~95% as seen in EDS analysis. The C–C, C═C, C═O, C═N functional groups were well-refuted from XPS spectra of carbon and oxygen elements in diamond. The interrelation between elements through FTIR analysis indicates major intrinsic bondings at 2687-2031 cm^{-1}. The aptasensing was evaluated through electrochemical impedance spectroscopy measurements, using NCP spiked human serum. With a good selectivity the lower detection limit was evidenced as 0.389 fM, at a linear detection range from 1 fM to 100 pM. The stability, and reusability of the aptasensor were demonstrated, showing ~30% and ~33% loss of active state, respectively, after ~11 days. The detection of NCP was evaluated by comparing anti-NCP aptamer and antibody as the bioprobes. The determination coefficients of $R^2 = 0.9759$ and $R^2 = 0.9772$ were obtained for aptamer- and antibody-based sensing, respectively. Moreover, the genuine interaction of NCP aptamer and protein was validated by enzyme linked apta-sorbent assay. The aptasensing strategy proposed with AuIDE/diamond enhanced sensing platform is highly recommended for early diagnosis of SARS-CoV-2 infection.

1. Introduction

SARS-CoV-2 is a sub-micron sized (~50–140 nm), belonging to Coronaviridae family in Nidovirales order. The virus has 50% genome similarity with MERS-CoV and 80% to SARS-CoV. Yet, the impact of SARS-CoV-2 transmission is the worst pandemic ever faced by the world in history. As of the mid 2021 umpteen cases were reported, SARS-CoV-2 has infected 175 million people and caused 3.8 million mortalities. These figures have not seen in the history that brought the world to its edge of life (WHO, 2021). At the early stage of disease spread, the virus was diagnosed using computed tomography (CT) scan, where the opacities in a patient's lung were compared with healthy lungs. Ahead of the virus sternness and the technology aroused in medical diagnosis, nucleic acid-based diagnoses were developed, having the reverse transcription-polymerase chain reaction (RT-PCR) as a key technique for detecting the virus (Lukose et al., 2021). However, RT-PCR is not applicable at the early stage of the virus attack with no symptoms, due to the negligible viral RNA multiplication in human. Moreover, it is compulsory to preserve RT-PCR kit at specific laboratory-based environment to retain the thermal cycler for PCR, which enables it for real-time or point-of-care (POC) diagnosis. The other detecting techniques developed in relation to RT-PCR are loop-mediated isothermal

* Corresponding author. Institute of Nano Electronic Engineering, Universiti Malaysia Perlis (UniMAP), 01000, Kangar, Perlis, Malaysia.
** Corresponding author.
E-mail addresses: subash@unimap.edu.my (S.C.B. Gopinath), zool@utm.my (Z.H. Ismail).

https://doi.org/10.1016/j.bios.2021.113735
Received 17 September 2021; Accepted 25 October 2021
Available online 27 October 2021

amplification (LAMP), and specific high-sensitivity enzymatic reporter unlocking (SHERLOCK) assay (Park et al., 2020). Yet, the performance of these techniques is not compatible with the real-time RT-PCR as it exhibits low sensitivity for the virus detection. Serological testing using sera is also highly proposed technique, yet its sensitivity reaches only ~65% of virus detection after 10 days of symptoms (Liu et al., 2021). With the regard, the effort to invent an outstanding detecting technique in diagnosing SARS-CoV-2 is never end as the effective early diagnosis of the disease is much needed to save millions of people worldwide. In addition to that, researchers are keen in inventing a home-based detecting kit as user-friendly in determining the existence and condition of virus infection in human body.

SARS-CoV-2 is composed of four main structural proteins; nucleocapsid (NCP), spike glycoprotein (S), envelope (E), and matrix (M). Among these, NCP is one of the early expressed proteins and has added a value in early diagnosis of the virus. As from the diagnosis of SARS-CoV-1, NCP can be detected in 24 h after the viral infection (Kiew et al., 2021). Besides than being the major viral replication component, it is also largely expressed and highly immunogenic during the infection (Taleghani and Taghipour, 2021). Therefore, detection systems with NCP of SARS-CoV-2 have highly been implemented with conventional enzyme-linked immunosorbent assay (ELISA) and many other immunoassays. Moreover, NCP as target was applied in immunoassays of detecting SARS-CoV-2, where NCP is utilized as a specific biomarker (Iravani, 2020). The immunoassay mechanism relies on the competitive binding affinity between target and probe, where either antibody or antigen can be fixed as a capture molecule. The immunoassays developed for SARS-CoV-2 detection often decides target protein as specific biomarker to be detected and the recombinant antibody as a bioprobe (Mojsoska et al., 2021). The emergence of molecule to be a counterpart for antibody known as aptamer, has shown excellent selective binding as antibody, and gained a huge attention as bioprobe in detecting proteins, small organic molecules, metals ions and whole cells. Aptamers can be generated as RNA or single-stranded DNA that provides either secondary or tertiary foldings for specific binding (Bezerra et al., 2019). Ahead of biosensor technology, aptamers are highly preferred as bioprobe due to its small sized structure, which makes it less immunogenic than antibody (Lakshmipriya and Gopinath, 2018). Aptamers are effortlessly synthesized using cost-effective method and it is easily modified as desired. Most importantly, aptamers can withstand at ambient and high temperatures, unlike antibodies which can undergo irreversible denaturation in room temperature. Moreover, aptamers can instantly reform to its original configurations as soon as its optimal condition is restored (Park, 2018). The remarkable advantages of aptamers have received significant attention in aptamer-based immunoassays in detecting viral RNA and proteins (Ramanathan et al., 2020).

Carbon-based materials are well-addressed in the state of art of biosensors and bio-imaging for disease diagnosis (Ramanathan et al., 2019, 2021). Carbon nanotubes, and graphene are well-known carbon-based materials with amazing electrochemical properties with fast electron transferring ability, as preferred for an ideal biosensing technology (Ginés et al., 2018). Diamond has its own breakthrough as one of the exciting carbon-based materials in the futuristic approach of bio-diagnostics. Diamond is a sp3 carbon composed material, which has been reported for good biocompatibility and bioactivity in the medical diagnostics and therapeutics. Among all carbon-based materials, carbon nanodiamond has emerged as a novel nanomaterial with highest biocompatibility, excellent fluorescent capacity, non-cytotoxic nature and a cost-effective large scale manufacturing (Basso et al., 2020; Mochalin et al., 2012). The capacity to track vacancies inside the diamond lattice using a laser crosses quantum theory and biology, where a groundbreaking capabilities for nanodiamonds in vivo practices are promised. Individual nanodiamonds can selectively interact with specific bio-agent, providing information on activities in a system and acting as a drug delivery vehicle. This gives a great bio-sensing platform as desired for ideal nano-diagnostics (Wu and Weil, 2017). Nanodiamonds have been justified as good bio-substrate in monitoring the cellular activities of bio-scaffold epithelial cells, tracking stress regions, uphold fluorescence in vivo imaging, and regulates the tension and immunity of desired biomolecule. Metal catalysts are not required for diamond synthesis, which are commonly utilized to produce other carbon-based nanomaterials. The absence of metal catalyst in the diamond further promotes biocompatibility with good cell viability and inhibit cell toxicity. Hence, diamonds are declared as inert in the biosensing as it eliminates the toxicity in an electrolyte system. With vast surface functional regions, the polar groups of nanodiamond provide an excellent platform in controlling the biomolecule adhesion. It plays huge significance with hydrophilic and hydrophobic domains of bio-environment (Chauhan et al., 2020; Kellens et al., 2018). The vitality of oxide groups in nanodiamond excel its electrocatalysis and electrical conductivity. The carbon and oxygen containing surface groups are denoted as the great advantageous to inhibit fouling due to its hydrophilic characteristics. The richness in the surface chemistry of nanodiamond are well utilized to perform ideal biosensing without biofouling and electrochemical fouling. As the research for extraordinary medical strategies are evolve, carbon nanodiamond are more prevalent.

A novel aptasensing strategy of targeting NCP using anti-NCP aptamer for SARS-CoV-2 detection has been proposed in the present research. High potential aptasensor for diagnosing SARS-CoV-2 was developed using gold interdigitated electrode (AuIDE) and its sensitivity was improved by incorporating carbon nanodiamond on the sensing surface. The inert diamond nanomaterial exhibits low-background current, high-current density, excellent electrochemical stability, and high-resistance to the fouling, which are extremely favorable in developing highly sensitive aptasensor (Kellens et al., 2018). The excellence of AuIDE empowers the sensing surface flexibility in producing high density bio-probe binding, aided by the large surface area/volume of carbon nanodiamond. The sudden emergence of SARS-CoV-2 has urged the development of specific binding aptamer for targeting the virus, as the bioprobe is still at its first crack. The presented research proposed a DNA aptamer structure desired specifically for detecting the NCP. The anti-NCP DNA aptamer was desired, procured and evaluated in the research in the development of high performance aptasensor in diagnosing SARS-CoV-2 infectious disease. The performance of developed aptasensor was determined by Electrochemical Impedance Spectroscopy (EIS) electrical characterization. EIS analyses are well-defined in the recent state-of-art of biosensor, especially in resulting exact impedance spectra and evaluation for precise changes of surface chemistry performed on a sensing surface (Ibau et al., 2020; Krishnan et al., 2021). With the regard, the intensity of anti-NCP aptamer and NCP specific binding on diamond enhanced AuIDE was validated through the impedimetric assessment. With all the above, the proposed aptasensing strategy is expected to be highly feasible for a fast and large-scale diagnostic technology for SARS-CoV-2, which is immensely needed to save the world from the worst pandemic.

2. Methodology

2.1. Diamond modification

Commercially purchased diamond nanopowder was produced by plasma chemical vapor deposition (PCVD) and high-pressure high temperature (HPHT). Thus, it exhibits several chemical functional groups on its surface. To tune the surface functional group as preferred for nanomaterial deposition on AuIDE, diamond nanopowder was modified using 1,1′-Carbonyldiimidazole (CDI) as a chemical linker. The procedures for diamond modification and its characterizations are included in supplementary details.

2.2. AuIDE sensing surface functionalization

The commercially procured AuIDEs were used as primary substrate for the sensor development. The AuIDE was characterized using scanning electron microscope (SEM, Hitachi, S-4300 SE, Japan), high power microscope (HPM), and 3D nanoprofiler (Hawk 3D Optical-Surface Profiler, South Korea) to examine the morphology of electrode fingers and its gap sizes. A series of chemical modification was performed to ensure the specific binding of NCP target on AuIDE. As the primary modification, an amino-silanization of hydroxyl groups was performed to form amine groups on the silicon substrate surface. Thus, 20 μL of 1% potassium hydroxide (KOH) solution was dropped on AuIDE surface and incubated for 15 min. The activation generates silanol groups (SiOH) on the native oxide layer of AuIDE by instantly oxidizing and covalently form bonding with hydroxyl (OH^-). Then, 20 μL of 2% (3-Aminopropyl) triethoxysilane (APTES) solution was dropped on the AuIDE surface and allowed incubation for 1 h. The hydroxyl terminated groups on AuIDE covalent bonds to the alkyl terminated group in APTES, resulting in amine-ends for diamond conjugation. As optimized silane layer forms on AuIDE, the unreacted APTES were washed using 10 mM Phosphate buffered saline (PBS). Afterward, 20 μL of CDI modified diamond solution was deposited on the sensing surface and incubated for 1 h. The modification steps of diamond using CDI is explained in the supplementary information. The CDI modified diamond exhibits ketone and epoxy groups, which have strong affinity with amine. Thus, the carbon nanodiamonds covalently form strong bonding with the AuIDE The diamond deposited sensing surface was thoroughly washed with PBS solution to ensure a uniform layer of nanomaterial deposition on AuIDE. Then, 20 μL of 1 μM amine-ended NCP aptamer was immobilized on AuIDE and incubated for 1 h. The sensing surface was then washed, and the unreactive active sites were blocked for 15 min using 1 M ethanolamine (ETA) to eliminate non-specific detections. The surface functionalization of AuIDE were performed at room temperature. The chemically modified AuIDE were stored at 4 °C prior to the NCP target detection using electrical characterization.

2.3. Electrochemical measurements: impedance spectroscopy

The electrochemical characterizations of AuIDE were examined through quantitative electrochemical impedance spectroscopy (EIS) using Novocontrol alpha high-frequency analyzer (Novocontrol Technologies GmbH, Germany). Redox solutions consist of 10 mM PBS, 5 mM of potassium hexacyanoferrate (III), $K_3[Fe(CN)_6]$ and 5 mM potassium hexacyanoferrate (II), $K_4[Fe(CN)_6]$, were used to characterize the impedance readings with EIS analysis. The EIS measurements were recorded at 100 mV_{RMS} amplitude of alternating current (AC) voltage supply with the frequency swept from 0.1 to 1 MHz. The impedance readings for bare AuIDE were recorded by dropping 20 μL of redox probe and run the analysis through WinDETA's Dielectric and Magnetic Material Measurement user software. Similarly, the impedance spectra for diamond modified AuIDE were recorded to determine the reproducibility of nanomaterial deposited AuIDE. The NCP protein and anti-NCP aptamer binding were interpreted by EIS readings. The NCP protein from 1 fM to 100 pM range of concentrations were prepared. The chemically modified AuIDE for protein detection was set at the EIS probe station. A 20 μL of 1 fM NCP target was interacted on the sensing surface and incubated for 5 min. Then, the surface was washed with PBS solution to remove the unbound target. As per Faradaic measurement, the redox solution was dropped on the sensing surface. The EIS reading on AuIDE with 1 fM was recorded. The detecting method of workings was performed from the lowest to the highest NCP concentrations. The impedance spectra were plotted for the real, Z' and imaginary parts, Z'' of impedance.

2.4. Enzyme linked apta-sorbent assay (ELASA)

The interaction of biomolecules on AuIDE gives measurement of an impedimetric signal on the basis of sensing device. Yet, the validation of disease causing agents and its probe is necessary to affirm the use of right biomarker to detect the target analyte. ELASA was performed to detect NCP using the desired anti-NCP aptamer as the validation assay for aptamer and target protein specific binding. The details of ELASA procedure are included in the supplementary information.

3. Result and discussion

The presented research proposes a promising strategy of detecting SARS-CoV-2 with AuIDE enhanced by carbon nanodiamond using EIS measurement. Being an early expressed protein, NCP was chosen as the target, whereas an anti-NCP aptamer was used as the probe to determine the fatal disease. The DNA aptamer desired and procured specifically for targeting NCP was evaluated for prompt and high performance aptasensor development. The aptasensing was improved by amino-silanization, followed by nanodiamond modification on AuIDE, which enables high density biomolecular immobilization. The binding of anti-NCP aptamer and target was quantitatively determined using EIS measurement. Fig. 1 shows the digital image of AuIDE and the schematic illustration of proposed strategy in detecting SARS-CoV-2 NCP by anti-NCP aptamer on diamond modified AuIDE. EIS gives a detailed information on the bio-molecules interaction takes place on the AuIDE and aids to determine the aptasensing performance between NCP and anti-NCP aptamer on the developed AuIDE. The section elaborates the aptasensing performance by discussing the result obtained through morphological (qualitative) and electrical (quantitative) characterizations.

3.1. Design and characterization of sensing platform

3.1.1. Physiochemical properties of diamond

The carbon nanodiamond was modified with CDI chemical linker to enable the activation of functional groups on the nanomaterial active surfaces. The chemically modified diamond was characterized for its morphological and structural validations. Fig. 2a shows the field emission transmission electron microscope (FETEM) image of diamond and the size of diamond evaluated from the image was ~20 nm. Fig. 2b reveal the spherical shape of carbon nanodiamond, observed through field emission scanning electron microscope (FESEM) imaging. Both FESEM and FETEM images revealed the uniformity of diamond size and shape. Moreover, it shows a uniform distribution on the imaging, although it was chemically modified from its original state. The elemental composition of diamond was identified through the energy disperse spectroscopy (EDS). Based on the EDS spectra shown in Fig. 2c, the diamond consist of ~95% of carbon element and the rest ~2 of % oxygen and nitrogen. The presence of platinum (Pt) in the spectra was came from the imaging method, where Pt was coated for better imaging results. The structural details of diamond were obtained from X-ray diffraction spectroscopy (XRD), X-ray photoelectron spectroscopy (XPS) and Fourier Transform Infrared Spectroscopy (FTIR) analyses. The detailed discussion of carbon nanodiamond structural analyses are presented in the supplementary material and the results are shown in Fig. 2d–h. The morphological and structural validations of carbon nanodiamond affirm its contribution in improving the performance of AuIDE, with its appealing nano-characteristics.

3.1.2. Diamond deposition and electrochemical properties

The electrochemical measurements were conducted using three AuIDE (n = 3) surfaces, as triplicates to emphasize the accuracy of reproducibility. The readings were compared between AuIDE and AuIDE deposited with carbon nanodiamond. The morphology of bare AuIDE is shown in Fig. 1a–c. The morphology examination reveals the exactness

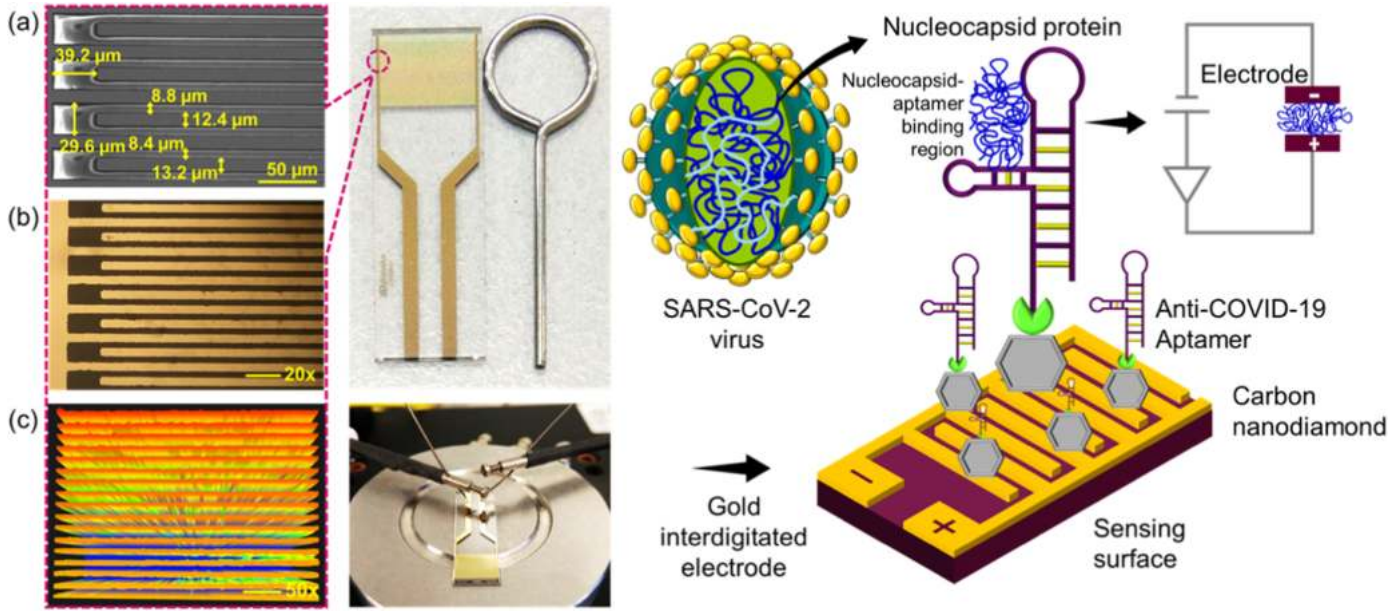

Fig. 1. Schematic illustration of NCP detection using anti-NCP aptamer on diamond enhanced AuIDE. The recombinant NCP and desired anti-NCP aptamer interaction was evaluated through impedimetric analysis by electrochemical spectroscopy. Morphological observations of AuIDE are shown, as characterized under (a) SEM, (b) HPM and (c) 3D-nanoprofiler. The measurements indicated in SEM image reveal the accuracy of AuIDE.

of finger and gap dimensions of the bare AuIDE. The deposition of diamond on AuIDE was evidenced by optical images (Fig. 3a–c). Fig. 3a and b shows the optical image of diamond deposited AuIDE under 3D profiler and HPM, respectively, whereas Fig. 3c revealed the 3D-view of sensing surface attached with the nanomaterial. These images validated the diamond deposition on the silicon oxide substrate in between the gold electrodes. Fig. 3d and e displays the Nyquist plots generated with EIS measurements obtained with and without diamond on AuIDE. The semicircle profile obtained by measuring bare AuIDE represents the Randles circuit, which express the redox solution resistance (R_s), charge transfer resistance (R_{ct}) and double layer capacitance (C_{dl}) (Taniselass et al., 2020). Fig. 3d(i) shows that the starting R_s for the three bare AuIDE were same, which indicate the exact reproducibility of the devices. The schematic shown in Fig. 3d represent bare AuIDE. The deposition of diamond on AuIDE generates two semicircles represent the equivalent circuit of the system (Fig. 3e). The equivalent circuit represent the small-perturbed semicircle (R_s with R_{ct1} parallel combination), which was in series with the large semicircle represent $R_{ct2}C_{dl2}$ parallel combination. Small semicircle represents the ion migration, whereas the mid-frequency range semicircle indicates the charge transfer in the system, denoted by R_{ct} and C_{dl}. The schematic illustration in Fig. 3e denotes the AuIDE modification with APTES and diamond deposition. The modification of AuIDE with APTES creates an apparent silane layer, which results the appropriate equivalent circuit. The principle of EIS equivalent circuits are reported in literatures (Li et al., 2021; Pajkossy et al., 2021). The appearance of two semicircles indicate the intercalation and de-intercalation on sensing platform. The high-frequency semicircle represents the capacitance and resistance exist with the silane layer. The second semicircle represent the charge exchange at the double layer, which indicated as double layer capacitance (C_{dl}) (Lukács and Kristóf, 2020). A computational equation have been used for fitting the equivalent circuit impedance data. Based on the literature, the below equation is used to compute the interface capacitance,

$$(Y_0 R_{ct})^{1/n} \sin\frac{n}{2}\pi = C_{dl}R_{ct}.$$

With the physical properties of diamond nanoparticle and AuIDE, the interface capacitance computed for the diamond deposited silane modified AuIDE is ~13 μF/cm^2, at the small semicircle and the second semicircle has an order of magnitude of ten thousands μF/cm^2. As reported in literature, C_{dl} for metal electrodes is ~20 μF/cm^2 (Frust et al., 2014). Thus, the calculation of interface capacitance indicates that the high-frequency semicircle represent the charge exchange state in the equivalent circuit. The computational analysis further validates the reliability of the diamond modified AuIDE with silane layer for NCP aptasensing strategy. The diamond deposited AuIDE reveal a high real and imaginary impedance (~600 Ω), whereas bare AuIDE exhibits low values (~50 Ω). The modification of AuIDE with APTES creates a resistive silane layer, which generates a high resistance and causes the drastic increment for the real part impedance. In addition, the unique properties of carbon nanodiamond enhances the capacitance and resistance of the sensing system, is demanded for high accuracy EIS measurements (Claudel et al., 2020; Mazlan et al., 2017). Prior to the pristine gold electrode sensing surface, the bare AuIDE reveals a low resistive layer, shown by the small Z' value. Although the diamond has been attached, the starting R_s for the three different AuIDEs deposited with diamond were similar [Fig. 3e(i)]. This indicates the accuracy of reproducibility (n = 3) and perfectness of surface chemistry and uniformity in depositing diamond in AuIDE. The slight variation was observed in the Nyquist plot diameter for the devices may aroused due to the contaminants existed on the sensing surface.

3.2. SARS-CoV-2 detection on Diamond-AuIDE

3.2.1. NCP and anti-NCP aptamer interaction

The Nyquist plots for AC impedance spectra were analyzed to determine the interaction between NCP and anti-NCP aptamer on diamond modified AuIDE. The impedance spectra were discussed based on the changes observed in the real part impedance, Z', which represents the intensity of electron transfer between the AuIDE interfacial layers. The depicted Z' value indicate the charge transfer resistance from the redox solution on the sensing surface. With the regard, the detection of NCP on developed AuIDE was evaluated based on the change of Z' values. Fig. S1 shows the schematic illustration of surface modification performed on AuIDE for detecting SARS-CoV-2 NCP as target. The success of surface chemistry on AuIDE is shown in Fig. S2, indicating the mean Z' versus the analyte added. As explained earlier, the modification of APTES on AuIDE generates a high resistive layer. The Nyquist plots

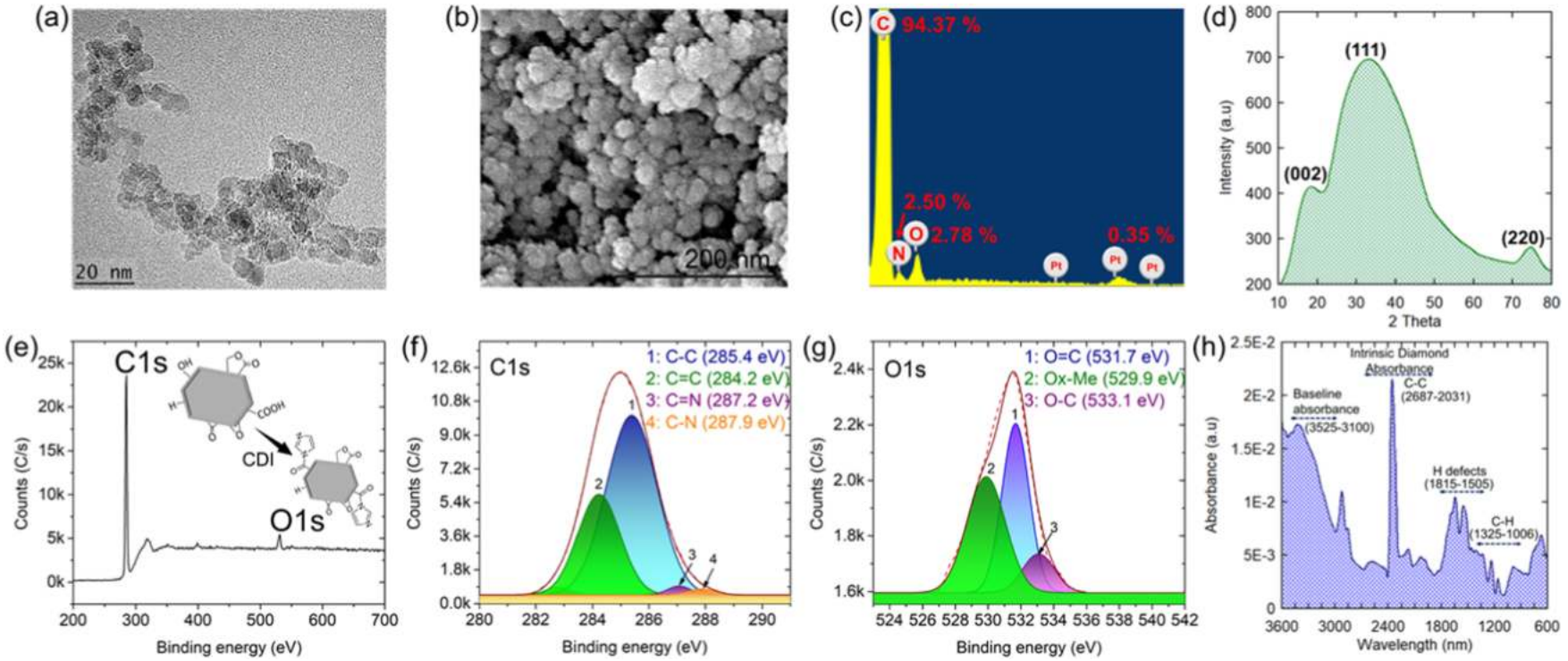

Fig. 2. Morphological and structural characterization of carbon nanodiamond. (a) FETEM image of diamond, showing ~20 nm sized diamond particles. (b) Spherical shape of diamond is apparently shown in FESEM image. (c) Elemental ratio of diamond, indicating ~95% of C with least amount of O and N. (d) XRD spectra of diamond, indicating three peaks with diffraction planes of (111), (220), and (002). (e) XPS survey spectra of diamond, reveal high counts for C and O with a low count. Deconvoluted XPS spectra of (f) C and (g) O, denote the chemical bonding present on the diamond surface. (h) FTIR spectra shows the chemical functional group present in the rigid tetrahedral structure of diamond.

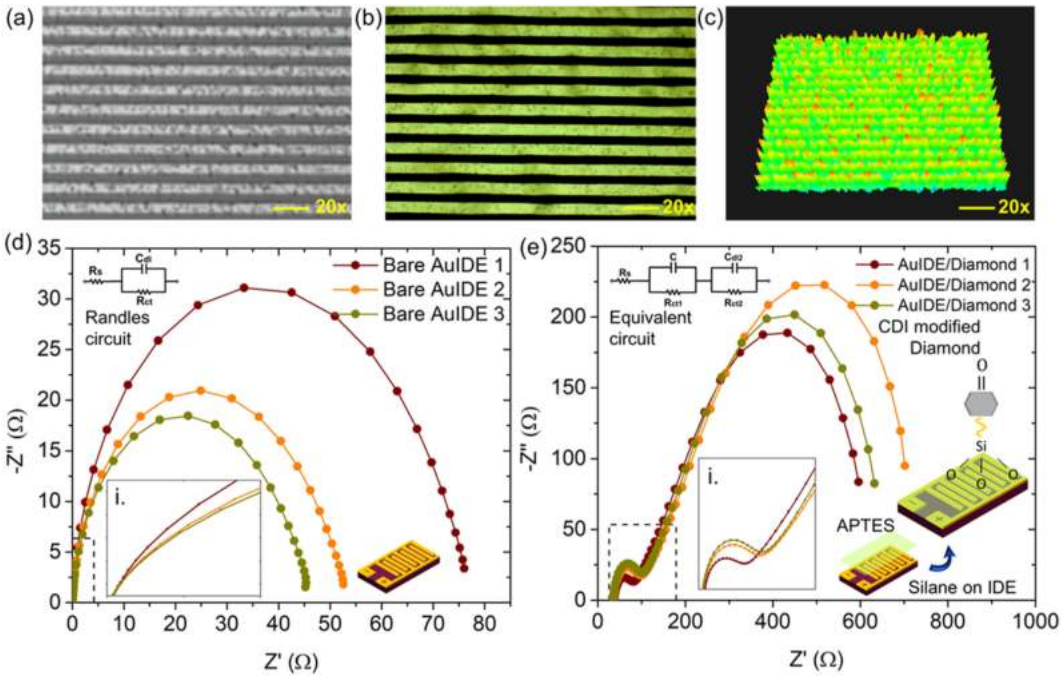

Fig. 3. Morphology and electrical characterization of diamond deposited AuIDE. The uniform distribution of carbon nanodiamond are determined by (a) 3D-optical microscope, (b) HPM and (c) 3D image of 3D nanoprofiler. Impedance spectra for three (d) bare AuIDE and (e) diamond deposited AuIDE, shows the reproducibility strength of both sensing surfaces. The inserted figures d(i) and e(i) shows the starting redox solution resistance (R_s) of the devices.

shown in Fig. S3 represents the EIS spectra of AuIDE from its activation with KOH, silane modification followed by nanomaterial deposition and aptamer-target immobilization. The subsequent deposition of diamond nanomaterial contributes to a slight elevation in the charge resistance between the interfacial layers of the sensing surface. The increment in the Z' value from 0.37 kΩ (diamond deposited AuIDE) to 0.47 kΩ upon anti-NCP aptamer immobilization describes the adsorption of probe on the modified AuIDE sensing surface. The high intensity of aptamer immobilization justifies the covalent bonding between diamond and aptamer. The aptamer immobilized device was characterized under Fourier Transform Infrared Spectroscopy (FTIR). The FTIR spectra (Fig. S4) justified the appropriate immobilization of aptamer on diamond deposited AuIDE. The increase of resistance caused by aptamer immobilization also explains the electrostatic repulsion caused by the electro-negative charge carried by the aptamer. The secondary structures of anti-NCP aptamers (Fig. S5) were predicted using web server for secondary structure prediction (https://rna.urmc.rochester.edu/RNAstructureWeb). A slight increase was observed with the blocking of sensing surface with ETA, explain the blocking of non-specific binding sites. In addition to the elimination of non-specific binding, blocking also creates a consistency in retaining the constant charge transfer resistance between the redox solution and the electrode sensing surface. This ensures that Z' immensity exhibit by the modified AuIDE is constant and specific regarding the biomolecule interaction of the sensing system. Upon NCP interaction, the increase on Z' (0.61 kΩ) elucidates target binding with aptamer and the ability of diamond modified AuIDE in recognizing the NCP target. The changes in the equivalent circle with two semicircles occurred due to the intercalation of well-matched DNA hybridization on the sensing platform. The complementary hybridization of DNA target and aptamer results in a series of covalent redox probe activation that interact with the base stack of the device. The redox probe encounter the electronic coupling, existed due to the DNA intercalation and rules the overall electrocatalytic kinetic in the electrolyte system (Jarczewska et al., 2016). The electrocatalytic kinetic unambiguously effects the electrochemical reduction of redox probe and empower the resistance and capacitance exhibited by the system. Hence, the DNA intercalation solely responsible for the changes in Nyquist plot semi-circles, in the presence of NCP targets (Le et al., 2015; Long et al., 2003). The surface modification of two-electrode system using carbon nanodiamond and its functionalization using anti-NCP aptamer ensured the stability of the developed aptasensor for accurate EIS measurements. Additional information was included in supplementary information.

3.2.2. *Aptasensing analysis of NCP*

Fig. 4a shows the Nyquist plot of anti-NCP aptamer immobilized on diamond modified AuIDE surface exposed to NCP target concentrations from 1 fM to 100 pM. The enlarged image shown in Fig. 4a(i) shows the Nyquist plot generated at the low frequency. As the concentration of NCP was increased from 1 fM to 100 pM, the Z' increased, indicate the binding of aptamer-protein on the modified sensing surface. ETA exhibit 0.5 kΩ of Z' and the value was increased to 0.55 kΩ at 1 fM. The small increment in the Z' value indicates that NCP and anti-NCP aptamer interaction has taken place on the diamond modified AuIDE. Following that, 10 fM and 100 fM of target exhibited similar range of Z' values (~0.58 kΩ). Approximately 1-fold higher Z' value was observed at 1 pM (0.68 kΩ) target from 1 fM, depict the notable accretion of aptamer-protein interaction. The Z' value linearly increased, and a large diameter semicircle was observed for 100 pM of target. The Z' value increases by 1.3-fold at 100 pM (0.77 kΩ) from 100 fM of NCP. The results denote that the lowest detection of NCP protein occurred at 1 fM and it elevates linearly up to 100 pM. The real part impedance increment upon increasing target concentrations explains the acceleration of charge transfer aroused with the innumerable anti-NCP aptamer and protein binding and its absorption on the diamond modified AuIDE. The analytical performance of developed aptasensor was evaluated with Bode plot analysis and the variation observed in phase angle. In accordance to the Faradaic impedance measurements, redox solution facilitates the electron transfer and promotes the electrochemical reactions, upon the supplied AC potential to the system. As the frequency swept, the system generates difference in phase angles, which results in capacitance and total impedance of the electrolyte system (Dorledo de Faria et al., 2019; Ferreira et al., 2020). According to the Warburg diffusion element, redox probe allows the solution resistance in series with charge transfer resistance and capacitance of the electrolyte

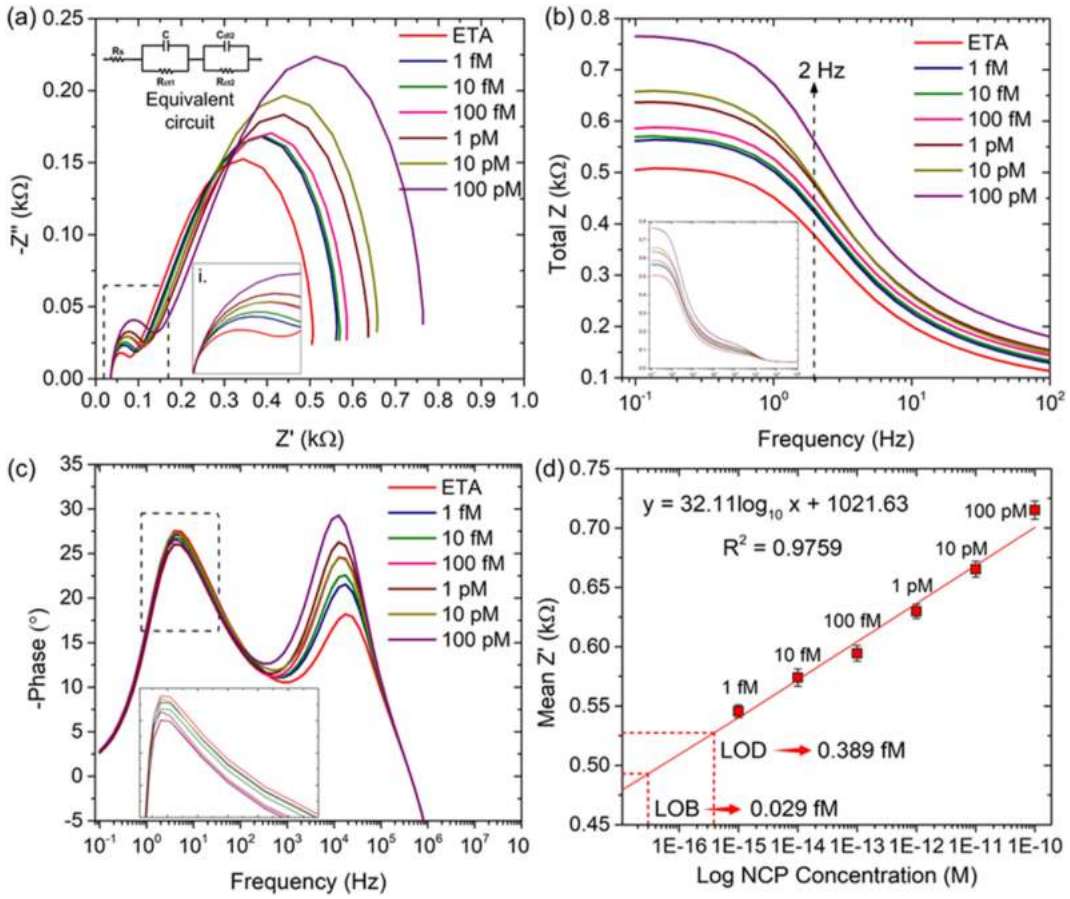

Fig. 4. Analytical performances of diamond incorporated AuIDE for detecting NCP. (a) Impedimetric spectra of diamond incorporated AuIDE. Immobilized with anti-NCP aptamer against NCP from the range of 1 fM to 100 pM. (b) Response total impedance. |Z| against the frequency, represent the Bode plot, where the equilibrium response of NCP detection observed at 2 Hz. The figure inset shows the overall |Z| response against frequency swept from 0.1 to 1 Mhz. (c) Phase angle versus the frequency plot shows two maximum phase angles. Indicating the equilibrium circuit system of the detection. (d) Calibration plot. Showing the linear regression for NCP from 1 fM to 100 pM with linear equation y = 32.11 $\log_{10}$ x + 0121.63 with regression coefficient of R_2 = 0.9759.

system, results equivalent circuit. With the facile electron transfer of redox probe, the EIS measurements obtain differences in phase angle at 45° and the total impedance as represented in Bode plot. With respect to the logarithmic frequency, the total impedance and phase angle differences were analyzed to determine the performance of developed aptasensor (Lukács and Kristóf, 2020; Strong et al., 2021). Fig. 4b shows the Bode plot generated with the total Z values against the frequency range supplied (0.1–1 MHz), where the total Z computed using the formula:

$$Z = \sqrt{(Z')^2 + (Z'')^2}$$

The Bode plot shows that the total 'Z' values increases from lowest to highest concentrations of NCP. It resembles the similar trend as Nyquist plot, indicating the increasing intensity of protein-aptamer binding on diamond modified AuIDE. As the magnitude of frequency supplied increases, the total 'Z' value decreases. It explains the high charge transferring system taken places at low frequency range (0.1–100 Hz). A stagnant 'Z' values were observed with all NCP concentrations after 10^4 Hz. This indicates that the sensing surface has achieved a passive state of response, where a fixed value of R_s was attained for all the targets immobilized. Fig. 4c shows the phase angle revealed by the diamond modified AuIDE with aptamer upon the interaction of NCP. The formation of two peak portions in the plot explain the two semicircles of Nyquist plot, indicating the equivalent circuit system. The maximum peak value occurred at 2 Hz is in good agreement with the active frequency range shown in the Bode plot (Fig. 4b) and the maximum phase angle shown in Fig. 4c. Thus, the real values of Z at 2 Hz were extracted to generate the calibration curve, and further evaluate the sensor performance. Fig. 4d shows the calibration curve plotted with the mean Z' values obtained at the 2 Hz versus logarithm of NCP concentrations. The linear calibration curve (n = 3) represents the linearity of diamond modified AuIDE in detection the NCP target from 1 fM to 100 pM. The linear equation obtained from the calibration curve is y = 32.11 log10 x + 1021.63. From that, the sensitivity of the AuIDE modified with diamond for the aptasensing of anti-NCP and NCP detection of 32.11 kΩ [log10 NCP (M)]. The linear equation was evaluated for computing the limit of blank (LOB) and the limit of detection (LOD) based on the quantification reported in (Taleuzzaman, 2018), shown as:

$$LoB = mean\ blank + 1.645(SD\ blank)$$

$$LoD = LoB + 1.645(SD\ low\ concentration\ sample)$$

Based on the computational evaluation, the LOD of the developed aptasensor modified with carbon nanodiamond is 0.389 fM for about 0.029 fM of LOB. The LOD attained in the presented research were compared with the reported work on detecting NCP (Table S1). Moreover, the correlation coefficient (R^2) of 0.9759 was obtained from the linear calibration curve, reveals the good performance of the developed aptasensor.

3.3. Selectivity assessment: NCP detection in spiked serum and cross-specificity

The strength of selectivity and specificity of diamond deposited

AuIDE with anti-NCP aptamer immobilized on it were evaluated. The potentiality of developed aptasensor in detecting NCP at clinical scale were determined using different NCP concentrations (1 fM to 100 pM) spiked in human serum. The concentration of stock human serum is 60 mg/ml. The diluted serum concentration used in the analysis was optimized by evaluating its impedance characterization upon reacting on anti-NCP aptamer immobilized sensing surface. As the impedance spectra of 1:10 human serum (6 mg/ml) is close to the ETA impedance response (Fig. S6), the concentration is chosen as it indicates its least response compared to the rest. Fig. 5a shows the Nyquist plot obtained by analyzing NCP spiked in human serum on diamond modified aptasensor. Similar to Fig. 4a, the detection range is prominent from 1 pM and Z' value reached 1.21 kΩ. The Z' value attained by 100 pM human serum diluted NCP was 1.37 kΩ, a 1.6-fold higher than 1 fM NCP diluted in PBS (0.87 kΩ). The accretion in Z' value indicates the large noise in the electrolyte system due to the presence of interference proteins in human serum (Hideshima et al., 2018). However, a linear detection Nyquist plot observed in Fig. 5a represents the excellence of diamond and anti-NCP aptamer on AuIDE in detecting NCP in human serum. The results justify the success of surface chemistry performed in developing the aptasensor as it creates an excellent anti-fouling layer on the sensing surface. The outstanding physiochemical properties of carbon nanodiamond on the silane layer have improved the reliability of the aptasensor using anti-NCP aptamer in detecting NCP targets diluted with human serum. The carbon nanodiamond vital surface functional groups and its electrocatalytic activity on the developed aptasensor eliminates the bio-fouling as it upholds high antifouling resistance. As the biomolecules adhere to the electrode surface, the polarity of nanodiamonds exhibit strong antifouling characteristics with its unique electrostatic and hydrophilic interactions. Human serum consist of intensive interference proteins and macromolecules with large molecular weights such as globulin (~66 kDa) and albumin (~150 kDa) (Purohit et al., 2020). The detection of NCP diluted in human serum at lower pico-molar range evidence the potentiality of the aptasensor for clinical applications. In an approach of real-time POC diagnostics of SARS-CoV-2, the developed aptasensor with carbon nanodiamond and anti-NCP aptamer as the bio-probe is expected to be satisfyingly sensitive to capture the NCP target among the interference proteins in serum, in the presented detection range.

The specificity of the aptasensor was analyzed to justify the ideal condition of sensor in detecting single and complementary target. The aptasensor was also interacted with 50 μL of 10 pM hemagglutinin (HA) of human influenza A, followed by 10 pM spike protein and then 10 pM NCP. The Z' values for the analysis are shown in Fig. 5b. The results denote that HA and spike protein gives no significant detection, whereas NCP gives specific detection. The results further justifies the specificity of aptamer in targeting only NCP and gives irrelevant results for non-specific targets. The stability and reusability of the developed aptasensor was evaluated to validate its performance and reliability for prompt and POC use. The results are shown Figs. S7 and S8 with its discussion included in the supplementary information. Moreover, the detection strength of diamond modified AuIDE with anti-NCP aptamer, was compared by immobilizing NCP antibody as probe. The aptasensor developed using antibody (Fig. S9) shows similar impedance

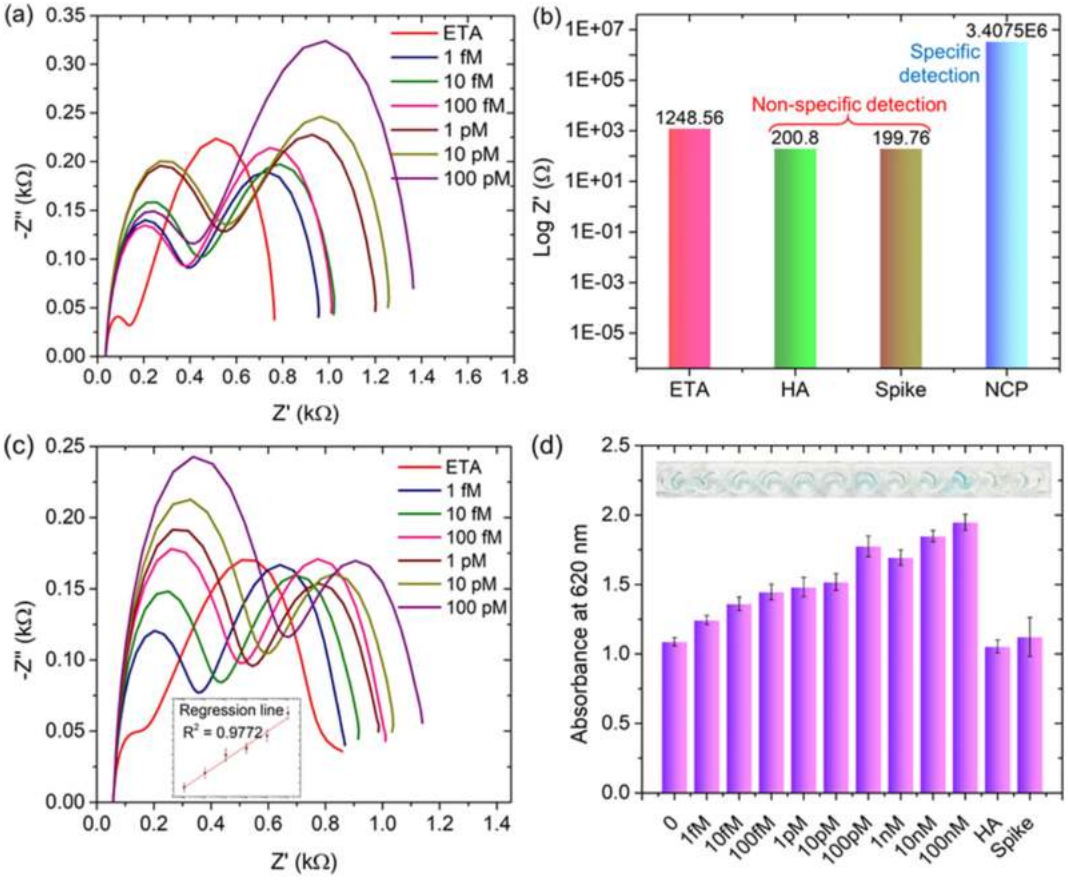

Fig. 5. Selectivity, specificity, stability and reusability assessments. (a) Impedimetric spectra of diamond incorporated AuIDE. Immobilized with anti-NCP aptamer against NCP diluted in serum. (b) Cross-specificity analyses of anti-NCP aptamer. Showing non-specific detection for non-specific protein. (c) Nyquist plot reveals the linear detection trend of NCP from 1 fM to 100 pM, using anti-NCP antibody as bioprobe on diamond modified AuIDE. Figure inset shows the calibration line with $R^2 = 0.9772$. (d) Absorbance reading of ELASA assay. Inserted digital image shows the color change in the wells. (For interpretation of the references to color in this figure legend, the reader is referred to the Web version of this article.)

characteristics (Fig. 5c) sustained by anti-NCP aptamer as bioprobe. In addition, the molecular validation of anti-NCP aptamer and its specific binding with NCP was determined (Fig. S10). Fig. 5d shows the ELASA results indicate binding affinity with the intensity of color change and the absorbance reading was at 620 nm. The results are further discussed in supplementary information.

4. Conclusion

The SARS-CoV-2 pandemic has required a great effort by the scientific research teams for curb the infectious disease wave around the world. This study succinctly demonstrated a high-performance aptasensor in detecting NCP of SARS-CoV-2 on the carbon nanodiamond enhanced AuIDE. The successful modification of nanomaterial on micro-sized AuIDE supports the high-density immobilization of anti-NCP aptamer for sensitive and reliable detection. The analytical performance of the developed aptasensor was determined through EIS measurement, which also validated the sensor configuration and stability. The success of the proposed aptasensing strategy was justified by the lower detection limit equal to 0.389 fM, with a linear detection range of 1 fM to 100 pM of NCP. The satisfactory performance of the developed aptasensor was determined through the selectivity, specificity, stability, and reusability of the device, which works well for the aimed fast, portable, and large-scale diagnostic techniques of SARS-CoV-2. The limitation of this study was the focus on surface modification with diamond, however, other multi-dimensional nanostructures with diverse modifications can be preferred for NCP detection at lower attomolar levels. Based on the conventional ELASA, the binding of aptamer-protein is significant for detecting NCP. Nevertheless, the conventional assay is not suitable for early and rapid detection of low concentrated NCP. Thus, the future work of the presented research may focus on developing ultrasensitive sensing surface using the advancement of multidimensional nanomaterials and advancement of aptamers in detecting NCP at low-cost.

Declaration of competing interest

The authors declare that they have no known competing financial interests or personal relationships that could have appeared to influence the work reported in this paper.

Acknowledgements

Authors acknowledge a grant (R.K130000.7343.4B617) under ASEAN University Network Southeast Asia Engineering Education Development Network (AUN/Seed-Net) Special Program for Research Against COVID-19 (SPRAC) and a grant (9001-00596) from Universiti Malaysia Perlis.

Appendix A. Supplementary data

Supplementary data to this article can be found online at https://doi.org/10.1016/j.bios.2021.113735.

References

Basso, L., Cazzanelli, M., Orlandi, M., Miotello, A., 2020. Appl. Sci. 10, 1–28. https://doi.org/10.3390/APP10124094.
Bezerra, G., Córdula, C., Campos, D., Nascimento, G., Oliveira, N., Seabra, M.A., Visani, V., Lucas, S., Lopes, I., Santos, J., Xavier, F., Borba, M.A., Martins, D., Lima-Filho, J., 2019. Anal. Bioanal. Chem. 411, 6667–6676. https://doi.org/10.1007/s00216-019-02040-5.
Chauhan, S., Jain, N., Nagaich, U., 2020. J. Pharm. Anal. 10, 1–12. https://doi.org/10.1016/j.jpha.2019.09.003.
Claudel, J., Ngo, T.T., Kourtiche, D., Nadi, M., 2020. Biosensors 10. https://doi.org/10.3390/bios10120208.
Dorledo de Faria, R.A., Dias Heneine, L.G., Matencio, T., Messaddeq, Y., 2019. Int. J. Biosens. Bioelectron. 5, 29–31. https://doi.org/10.15406/ijbsbe.2019.05.00148.
Ferreira, P.A.B., Araujo, M.C.M., Prado, C.M., de Lima, R.A., Rodríguez, B.A.G., Dutra, R. F., 2020. Colloids Surf. B Biointerfaces 189, 110834. https://doi.org/10.1016/j.colsurfb.2020.110834.
Frust, A., Hill, M.G., Barton, J.K., 2014. Electrocatalysis 23, 1–7. https://doi.org/10.1016/j.poly.2014.07.005.
Ginés, L., Mandal, S., Morgan, D.J., Lewis, R., Davies, P.R., Borri, P., Morley, G.W., Williams, O.A., 2018. ACS Omega 3, 16099–16104. https://doi.org/10.1021/acsomega.8b02067.
Hideshima, S., Wustoni, S., Kobayashi, M., Hayashi, H., Kuroiwa, S., Nakanishi, T., Osaka, T., 2018. Sens. Bio-Sensing Res. 17, 25–29. https://doi.org/10.1016/j.sbsr.2018.01.003.
Ibau, C., Arshad, M.K.M., Gopinath, S.C.B., Nuzaihan, M., Fathil, M.F.M., Shamsuddin, S. A., 2020. Int. J. Biol. Macromol. 162, 1924–1936. https://doi.org/10.1016/j.ijbiomac.2020.08.125.
Iravani, S., 2020. Mater. Adv. 1, 3092–3103. https://doi.org/10.1039/d0ma00702a.
Jarczewska, M., Górski, Ł., Malinowska, E., 2016. Anal. Methods 8, 3861–3877. https://doi.org/10.1039/c6ay00499g.
Kellens, E., Bové, H., Vandenryt, T., Lambrichts, J., Dekens, J., Drijkoningen, S., D'Haen, J., Ceuninck, W., Thoelen, R., Junkers, T., Haenen, K., Ethirajan, A., 2018. Biosens. Bioelectron. 118, 58–65. https://doi.org/10.1016/j.bios.2018.07.032.
Kiew, L.V., Chang, C.Y., Huang, S.Y., Wang, P.W., Heh, C.H., Liu, C. Te, Cheng, C.H., Lu, Y.X., Chen, Y.C., Huang, Y.X., Chang, S.Y., Tsai, H.Y., Kung, Y.A., Huang, P.N., Hsu, M.H., Leo, B.F., Foo, Y.Y., Su, C.H., Hsu, K.C., Huang, P.H., Ng, C.J., Kamarulzaman, A., Yuan, C.J., Shieh, D. Bin, Shih, S.R., Chung, L.Y., Chang, C.C., 2021. Biosens. Bioelectron. 183, 113213 https://doi.org/10.1016/j.bios.2021.113213.
Krishnan, H., Gopinath, S.C.B., Md Arshad, M.K., Zulhaimi, H.Ii, Ramanathan, S., 2021. Microchim. Acta 188, 1–12. https://doi.org/10.1007/s00604-021-04794-1.
Lakshmipriya, T., Gopinath, S.C.B., 2018. INNOSC Theranostics Pharmacol. Sci. 1, 14–19. https://doi.org/10.26689/itps.v1i1.511.
Le, M.H., Jimenez, C., Chainet, E., Stambouli, V., 2015. Sensors 15, 10686–10704. https://doi.org/10.3390/s150510686.
Li, X., Qin, Z., Fu, H., Li, T., Peng, R., Li, Z., Rini, J.M., Liu, X., 2021. Biosens. Bioelectron. 177, 112672 https://doi.org/10.1016/j.bios.2020.112672.
Liu, P.P., Zong, Y., Jiang, S.P., Jiao, Y.J., Yu, X.J., 2021. ACS Omega 6, 9667–9671. https://doi.org/10.1021/acsomega.1c00253.
Long, Y.T., Li, C.Z., Kraatz, H.B., Lee, J.S., 2003. Biophys. J. 84, 3218–3225. https://doi.org/10.1016/S0006-3495(03)70046-0.
Lukács, Z., Kristóf, T., 2020. Electrochim. Acta 363. https://doi.org/10.1016/j.electacta.2020.137199.
Lukose, J., Chidangil, S., George, S.D., 2021. Biosens. Bioelectron. 178, 113004 https://doi.org/10.1016/j.bios.2021.113004.
Mazlan, N.S., Ramli, M.M., Abdullah, M.M.A.B., Halin, D.S.C., Isa, S.S.M., Talip, L.F.A., Danial, N.S., Murad, S.A.Z., 2017. AIP Conf. Proc. https://doi.org/10.1063/1.5002470, 1885.
Mochalin, V.N., Shenderova, O., Ho, D., Gogotsi, Y., 2012. Nat. Nanotechnol. 7, 11–23. https://doi.org/10.1038/nnano.2011.209.
Mojsoska, B., Larsen, S., Olsen, D.A., Madsen, J.S., Brandslund, I., Alatraktchi, F.A., 2021. Sensors 21, 1–11. https://doi.org/10.3390/s21020390.
Pajkossy, T., Urs Ceblin, M., Mészáros, G., 2021. J. Electroanal. Chem. 115655 https://doi.org/10.1016/j.jelechem.2021.115655.
Park, K.S., 2018. Biosens. Bioelectron. 102, 179–188. https://doi.org/10.1016/j.bios.2017.11.028.
Park, M., Won, J., Choi, B.Y., Lee, C.J., 2020. Exp. Mol. Med. 52, 963–977. https://doi.org/10.1038/s12276-020-0452-7.
Purohit, B., Vernekar, P.R., Shetti, N.P., Chandra, P., 2020. Sensors Int. 1, 100040 https://doi.org/10.1016/j.sintl.2020.100040.
Ramanathan, S., Gopinath, S.C.B., Arshad, M.K., 2020. Sci. Rep. 10 https://doi.org/10.1038/s41598-020-60208-x.
Ramanathan, S., Gopinath, S.C.B., Md, Arshad, M.K., Poopalan, P., 2019. Biosens. Bioelectron. 141, 111434 https://doi.org/10.1016/j.bios.2019.111434.
Ramanathan, S., Poopalan, P., Gopinath, S.C.B., Md Arshad, M.K., Anbu, P., Lakshmipriya, T., Salimi, M.N., Pandian, K., 2021. Mater. Chem. Phys. 265, 1–11. https://doi.org/10.1016/j.matchemphys.2021.124486.
Strong, M.E., Richards, J.R., Torres, M., Beck, C.M., La Belle, J.T., 2021. Biosens. Bioelectron. 177, 112949 https://doi.org/10.1016/j.bios.2020.112949.
Taleghani, N., Taghipour, F., 2021. Biosens. Bioelectron. 174, 112830 https://doi.org/10.1016/j.bios.2020.112830.
Taleuzzaman, M., 2018. Org. Med. Chem. IJ 7, 555722. https://doi.org/10.19080/OMCIJ.2018.07.555722.
Taniselass, S., Arshad, M.K.M., Gopinath, S.C.B., Ramli, M.M., 2020. J. Colloid Interface Sci. 577, 345–354. https://doi.org/10.1016/j.jcis.2020.05.070.
WHO, 2021. WHO coronavirus (COVID-19) dashboard. Who. URL. https://covid19.who.int/.
Wu, Y., Weil, T., 2017. Phys. Sci. Rev. 2, 1–17. https://doi.org/10.1515/psr-2016-0104.